### To be published in Optics Letters:

Title: Real-time wide-field spectral-scanning FMCW coherent 3D imaging and

velocimetry

**Authors:** Jingkai Zhang, Joseph Izatt, Al-Hafeez Dhalla, Ruobing Qian, Kevin Zhou, Christian

Viehland, Mark Draelos

Accepted: 20 July 22

Posted 20 July 22

**DOI:** https://doi.org/10.1364/OL.463965

© 2022 Optica

# **OPTICA** Publishing group

Formerly OSA

## Real-time wide-field spectral-scanning FMCW coherent 3D imaging and velocimetry

JINGKAI ZHANG,<sup>1</sup> RUOBING QIAN,<sup>1</sup> KEVIN C. ZHOU,<sup>1</sup> CHRISTIAN VIEHLAND,<sup>1</sup> MARK DRAELOS,<sup>1</sup> AL-HAFEEZ DHALLA,<sup>1</sup> AND JOSEPH A. IZATT,<sup>1,2,\*</sup>

Received XX Month XXXX; revised XX Month, XXXX; accepted XX Month XXXX; posted XX Month XXXX (Doc. ID XXXXX); published XX Month XXXX

We present a novel real-time spectral-scanning frequency-modulated continuous wave (FMCW) 3D imaging and velocimetry system that can produce 3D depth maps at 33 Hz, with 48° X 68° field of view (FOV) and 32.8 cm depth range. Each depth map consists of 507 X 500 pixels, with 0.095° X 0.14° angular resolution and 2.82 mm depth resolution. The system employs a grating for beam steering and a telescope for angular field of view (FOV) magnification. Quantitative depth, reflectivity and axial velocity measurements of a static 3D printed depth variation target and a moving robotic arm are demonstrated. © 2022 Optica Publishing Group

Three-dimensional (3D) surface imaging with high speed and high resolution is sought after in many current and developing technical fields, such as virtual reality, robotic vision, facial recognition, biomedical imaging and autonomous driving. 3D surface imaging acquires pixels with depth information in a 3D scene. While many 3D surface imaging approaches have been developed over the years, recently Light Detection and Ranging (LiDAR) has become increasingly popular, primarily motivated by the autonomous driving industry.

Frequency-modulated continuous wave (FMCW) LiDAR is an emerging form of LiDAR which shares the same working principle as swept-source optical coherence tomography (SSOCT). In comparison with SSOCT, FMCW LiDAR designs typically prioritize long imaging range over high axial resolution, and employ a peak reflector detection algorithm to condense the axial dimension into a single depth measurement for each pixel[1,2]. As a coherent continuous wave (CW) imaging system, FMCW LiDAR offers some advantages over pulsed direct detection systems such as Time of Flight (ToF) LiDAR[3,4] and Amplitude-modulated continuous wave (AMCW) LiDAR. These advantages include superior resolution and much higher immunity to optical interference such as ambient light or other nearby LiDAR systems compared to both ToF[5,6] and AMCW[7] LiDAR systems.

In our previous work[8], we demonstrated FMCW LiDAR for real-time room-scale 3D surface imaging using non-mechanical

(grating-based) lateral scanning. The imaging range of an FMCW LiDAR or an SSOCT system is generally limited by the instantaneous coherence length of the laser source, which is inversely proportional to the instantaneous laser linewidth[9]. An emerging application for FMCW and SSOCT approaches is meter scale imaging for room-scale applications, such as robotic vision and facial recognition, as opposed to 10-100 meters range which is required for autonomous driving applications[1,10]. Several laser technologies have been reported for meter-scale imaging: verticalcavity surface emitting lasers (VCSEL)[11-13], optical timestretching[14,15], Fourier-domain mode locking (FDML)[16], single or stitched distributed feedback (DFB)[6,17], and akinetic allsemiconductor programmable lasers[10]. These technologies can increase the SSOCT/FMCW LiDAR imaging range to several meters. However, achieving a larger imaging range without sacrificing depth resolution requires either an equivalent increase in detector bandwidth or in acquisition time. Even using GHz bandwidth detection, it requires seconds to hours to acquire a single depth image with hundreds of points in lateral dimensions and tens of centimeters in imaging range with micrometer-scale axial resolution[10,17].

Traditional mechanical scanners used in OCT and LiDAR usually have a maximum scan rate of a few kHz, which practically limits the frame rate of raster scanning 3D imaging systems that utilize dual scanners to a few Hz. Strategies to optimize scan patterns, such as spiral scanning[18], can improve scan efficiency by balancing the scan load between the orthogonally scanning mirrors, but these approaches introduce other drawbacks such as non-cartesian sampled data. Other nonmechanical, compact beam scanners are under development, such as optical phased arrays (OPAs), which steer beams by controlling the relative phase of coherent optical emitter arrays[19]. Unfortunately, practical OPAs developed to date suffer from large spatial sidelobes away from the design wavelength, limiting their use in low coherence interferometry applications[20]. Another approach is to use diffractive optics, such as diffraction gratings, to perform spectrally encoded spatial scanning[21,22]. Using a combination of a transmissive grating and a single-axis galvanometer mirror as the scanner, our previous

<sup>&</sup>lt;sup>1</sup>Department of Biomedical Engineering, Duke University, Durham, NC, USA, 27708, USA

<sup>&</sup>lt;sup>2</sup>Department of Ophthalmology, Duke University Medical Center, Durham, North Carolina 27710, USA

<sup>\*</sup>Corresponding author: joseph.izatt@duke.edu

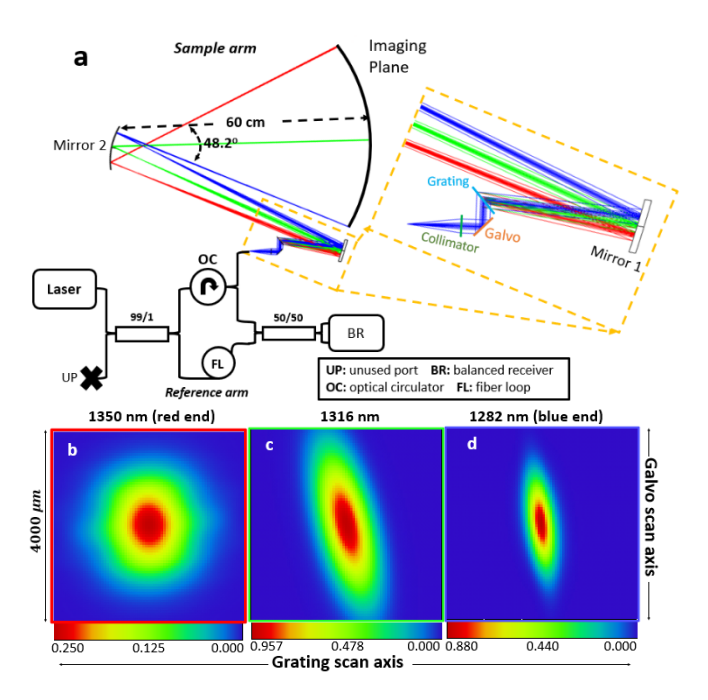


**Fig. 1.** (a) Schematic diagram of the system design, including sample arm Zemax design detail. UP: unused port, BR: balanced receiver, OC: optical circulator, FL: fiber loop. Red, green, blue line colors represent 1350nm, 1316nm, 1282nm wavelength. Zemax Huygens point spread function (PSF) model at the image plane for (b) 1350nm, (c) 1316nm, and (d) 1282nm wavelength. Colormap represents

system[8] performed 475 depth measurements along the spectral scanning axis within a single laser sweep, which corresponded to a depth voxel acquisition rate of 7.6 MHz. This system achieved an imaging range of 32.8 cm and a depth map frame rate of 33.2 Hz. However, the angular field of view (FOV) in the grating axis was only  $7.1^{\circ}$ , limited by the dispersion of the transmissive grating.

Thus, to broaden the applicability of our method, we here report an improved design of our FMCW 3D imaging system which extends the angular FOV in the grating axis to 48.2° by adding a custom-designed Keplerian reflective telescope. The schematic of the system design is shown in Fig. 1(a), including a ray-traced optical model (OpticStudio, Zemax, Kirkland, WA) of the sample arm. The light source was an akinetic all-semiconductor programmable swept laser source (Insight Photonics Solutions; Lafayette, CO) with a sweep range from 1282nm to 1350nm and a sample incidence power of 44mW. This power is compliant with the IEC 60825-1[23] class 1 limit conservatively calculated at the short wavelength end of the laser sweep range. Light from the source was separated into sample and reference arms by a 99/1 2x2 fiber coupler (Thorlabs; Newton, NJ). 1% was directed to the reference arm, while 99% progressed to the first port of an optical circulator which directed light to the sample arm. In the reference arm, light was transmitted through a precision length optical fiber before being directed to a 50/50 coupler. In the sample arm, light emerging from the sample fiber was collimated by an off-axis parabolic reflective collimator before being scanned by a 16mm aperture galvanometer mirror (Pangolin; Sanford, FL), which performed the slow axis beam scanning. A transmissive grating (1145 grooves/mm, Wasatch Photonics; Logan, UT) was positioned immediately after the galvanometer to perform spectrally-encoded fast axis beam scanning[8,22]. Afterwards, a Keplerian reflective telescope with an angular magnification of 6.8x extended the lateral angular FOV. The telescope consisted of a 2-inch off-axis parabolic mirror (Edmund Optics; Barrington, NJ) with effective focal length (EFL) of 516.8 mm, and a 3-inch concave mirror (Thorlabs; Newton, NJ) with EFL of 75 mm. Reflected light from the object was collected by the sample arm fiber and directed back to the circulator. The circulator, in turn, directed the sample light to the 50/50 fiber coupler, where the reference and sample reflection light was recombined. The interference signal was measured using a 400 MHz balanced photodetector (Insight Photonics Solutions; Lafayette, CO) and digitized at a sample rate of 800MS/s using an ATS 9373 digitizer (Alazar Technologies; Pointe-Claire, QC, Canada) to achieve an imaging depth range of approximately 32 cm. In the following discussion, we define the lateral dimension that is parallel to the direction of the grating diffraction as 'horizontal' and the lateral dimension that is perpendicular to the grating diffraction as 'vertical'. The horizontal angular FOV in the fast-scanning axis (grating scan axis) was 48.2°, and the vertical angular FOV in the slow scanning axis (galvo scan axis) was 68°, both limited by the aperture size of the telescope.

For a single 3D depth map, we acquired 50863 x 500 data points, where 50863 was the number of spectral sampling points per laser sweep (horizontal axis) and 500 was the number of laser sweeps (vertical axis). To estimate reflector depth as a function of lateral position, we applied overlapping short-time Fourier Transforms (STFTs) in the spectral scanning dimension, where the window size dictates the axial resolution and (in combination with the optical

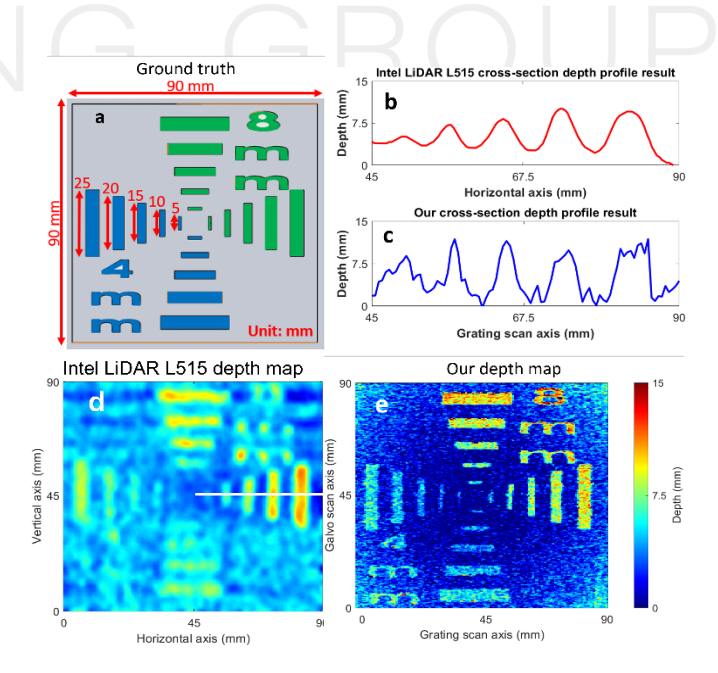


**Fig. 2.** (a) Schematic of the 3D printed depth target. Green color represents a recess of 8mm depth. Blue color represents a recess of 4mm depth. (b) Cross-section depth profile plot of the white line in (d). (c) Cross-section depth profile plot of the white line in (e). (d) Depth map of the depth target acquired by Intel RealSense L515 LiDAR. (e) Depth map of the depth target acquired by our FMCW 3D imaging system (Gaussian filtered and distortion corrected). Both (d) and (e) share the same colormap.

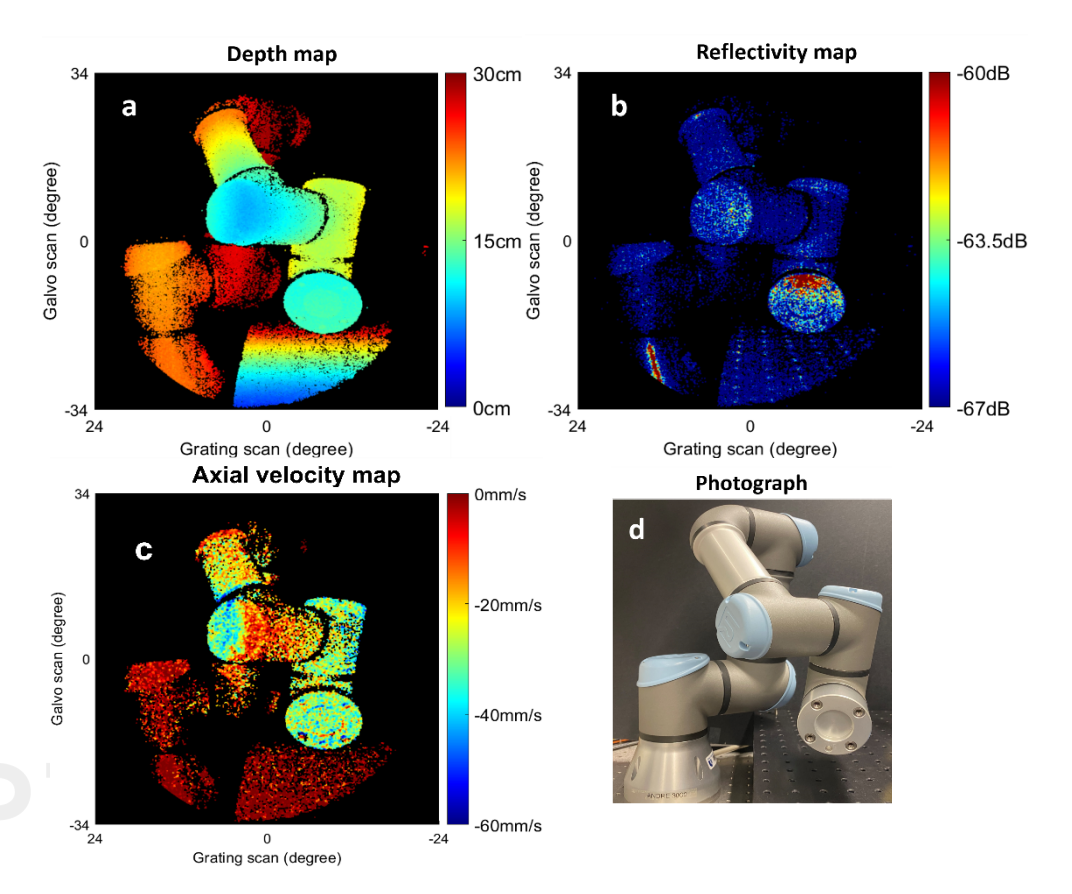


Fig. 3. (a) 3D depth map of a UR3 robot arm. (b) Reflectivity map of the UR3 robot arm. (c) Axial velocity map of the UR3 robot arm. (d) Real photograph of the UR3 robot arm.

transfer function) the lateral resolution along the grating dimension. We set the STFT window size to be 200 spectral sampling points or 0.27nm in wavelength at ~1316nm, allowing a 100-point overlap between adjacent spectral windows. We chose this window size based on a rational basis that if the point spread functions (PSFs) of two adjacent wavelengths are unresolvable (overlapping), the detected signals from these two wavelengths can be treated as arising from essentially the same object position, and should be included into the same STFT window. Then for each STFT window. we zero-padded the detected signal from 200 to 5000 points and applied the Fourier Transform, for sinc-interpolated, sub-pixel accuracy[8]. We employed peak reflection thresholding to find the peak location for each Fourier transformed STFT window, where the peak location identifies the depth of the principal reflection. Therefore, after STFT, we ended up with a 507x500 depth map, which was acquired in 0.03 sec or at 33 Hz. A linear distortion correction was applied in image post-processing to compensate for the image plane curvature.

As our sample arm is non-telecentric, it is helpful to define our lateral resolution in both angular (degrees) and distance units (mm). The horizontal angular FOV was  $48.2^{\circ}$ , evenly distributed across 507 pixels along the grating scan axis, giving a horizontal angular resolution of  $0.095^{\circ}$ . Similarly, the vertical angular resolution was  $68^{\circ}/500 \approx 0.14^{\circ}$ . On the other hand, we define horizontal and vertical distance resolution on an image plane that is 60 cm away from the last optic, as illustrated in Fig. 1(a). Fig. 1(b-d) demonstrate that the PSF at the image plane varied in size across

the grating scan axis, which caused the horizontal and vertical distance resolution to vary across the grating scan axis. However, the effect of this variation on the sensitivity of the signal across the FOV, as observed in Fig. 3(b), appeared to be small. Thus, the horizontal resolution, determined by the sum of PSFs of all the wavelengths within the same STFT window, varied between  $\sim 1.95$  mm and 3.17 mm, defined as the full width at half maximum (FWHM) of the intensity PSF. The vertical resolution, determined solely by the imaging optics, varied between  $\sim 1.37$  mm to 2.06 mm FWHM. The axial (depth) resolution is calculated using  $l_c=2ln2$   $(\lambda_0^2)/\pi\Delta\lambda$  [9] (same expression as conventional OCT axial resolution), to be 2.82 mm. The bandwidth  $\Delta\lambda$  in this calculation was the bandwidth of a single STFT window, equals to 0.27 nm.

We demonstrate FMCW 3D imaging results of two different objects: a custom 3D printed depth target and a UR3 commercial robot arm (Universal Robots; Denmark). The 3D depth target had an overall dimension of 90 mm x 90 mm and included recessed groove-shaped features of two different depths: 4mm and 8mm. The recessed grooves all had the same length to width ratio of 5 with various sizes across lateral axes in order to test 3D imaging system performance in all three dimensions. The length of each recessed groove is marked in Fig. 2(a). Fig. 2(d) and (e) compares the depth maps of the 3D depth target acquired by an Intel RealSense L515 LiDAR camera (Intel; Santa Clara, CA) and our FMCW 3D imaging system. In our experiment, we maximized the Intel LiDAR's resolution up to 1024 X 768 pixel per depth map and minimized its depth range to 30cm. The Intel LiDAR was chosen as

a basis for comparison because it is a current state of the art commercial room-scale ToF LiDAR device with similar FOV and frame rate to our system. Fig. 2(b) and (c) plot a cross-sectional depth profile of a single slice through the 3D data in Fig. 2(d) and (e), respectively. Although our depth profile is noisier than the L515 depth profile, our depth profile clearly resolves the feature edges. Our depth map unambiguously shows the '4mm' letters and can distinguish all recessed grooves. However, the Intel L515 LiDAR is not capable of imaging the '4mm' letters and the smallest recessed grooves. These comparisons demonstrate that our system can achieve better lateral and axial resolution than a current commercial room-scale LiDAR.

To demonstrate that our system's expanded FOV supports imaging dynamic meter-scale objects, Fig. 3(a) shows a singleframe of a depth map video of a UR3 robot arm (Universal Robots; Denmark) acquired by our system. The UR3 robot arm has 6 axes with a working radius of 500mm. We have also included a 33-fps depth map video of the robot arm making a complex movement as Visualization 1 in the supplemental material. demonstrate the ability to acquire quantitative reflectivity simultaneously, we show a reflectivity map of the UR3 robot arm in Fig. 3(b) and a 33-fps reflectivity map video as Visualization 2, processed from the same data acquisition as the depth map in Fig. 3(a). We also show a single frame axial velocity map in Fig. 3(c), and 33-fps axial velocity map video as Visualization 3 in the supplemental material, both obtained from a separate experiment with the robot end effector constrained to move directly toward the FMCW system aperture.

The reflectivity was defined and calculated  $R=20log_{10}~(E_{obj}/E_{mirror})+A$ , where  $E_{obj}$  is the measured peak location amplitude of the interferogram after STFT when measuring a real object, and  $E_{mirror}$  and A are factors derived from a calibration experiment. Specifically,  $E_{mirror}$  was the measured peak location amplitude of the interferogram after STFT when measuring a mirror in series with a neutral density filter (ND filter), and A is the round-trip attenuation of the ND filter used to attenuate the signal from the mirror. A is given by the equation:  $A=2\times 10log_{10}~(P_1/P_0)$ , where  $P_1$  is the measured optical power before the ND filter, and  $P_0$  is the measured optical power after the ND filter.

For the axial velocity measurement, we programmed the robot arm to move its end effector axially towards the FMCW system at a speed of 20 mm/s, while measuring 120 consecutive frames of depth maps at 33-fps. Since the end effector motion per frame at this velocity was less than the FMCW system axial resolution (2.82mm), we calculated the axial velocity per frame by dividing the measured axial displacement over sequential sets of 10 frames, divided by the acquisition time of 10 frames. A single frame of axial velocity is included in Fig. 3(c), and a 33-fps axial velocity map video as Visualization 3 is provided in the supplemental material. Using this methodology, the minimum detectable axial velocity and the axial velocity accuracy are 9.305 mm/s, and the theoretical maximum measurable axial velocity is 10.56 m/s. We did not employ the traditional doppler shift method[24] to measure velocity because our laser only sweeps in one direction.

The depth range in our system is currently limited by two factors: the Rayleigh range of the sample beam and the speed of our receiver. Faster receivers (and supporting digitizers) are commercially available and could potentially double or even triple the depth range of the system. However, these improvements would only be worthwhile if they were accompanied by modifications to the

system to improve the Rayleigh range. Such improvements are possible, albeit at the expense of lateral resolution and/or lateral FOV. Naturally, the trade-off between these design parameters should be driven by the application requirements.

**Acknowledgments.** This work was supported in part by NIH EY028079 (C.V., A.-H. D., J.A.I.), NSF CBET-1902904 (K.C.Z), and DOD CDMRP W81XWH-16-1-0498 (R.Q.).

**Disclosures.** The authors declare no conflicts of interest.

**Data availability.** Data underlying the results presented in this paper are available from the authors on reasonable request.

#### References

- 1. J. Riemensberger, A. Lukashchuk, M. Karpov, W. Weng, E. Lucas, J. Liu, and T. J. Kippenberg, Nature 581, 164 (2020).
- 2. A. Dieckmann, Electronics Letters 30, 308 (1994).
- M.-C. Amann, T. M. Bosch, M. Lescure, R. A. Myllylae, and M. Rioux, Optical engineering 40, 10 (2001).
- G. Berkovic and E. Shafir, Advances in Optics and Photonics 4, 441 (2012).
- B. Behroozpour, P. A. Sandborn, M. C. Wu, and B. E. Boser, IEEE Communications Magazine 55, 135 (2017).
- 6. X. Zhang, J. Pouls, and M. C. Wu, Optics express 27, 9965 (2019).
- D. J. Lum, S. H. Knarr, and J. C. Howell, Optics express 26, 15420 (2018).
- 8. R. Qian, K. C. Zhou, J. Zhang, C. Viehland, A.-H. Dhalla, and J. A. Izatt, Nature Communications 13, 1476 (2022).
- J. A. Izatt, M. A. Choma, and A.-H. Dhalla, in Optical Coherence Tomography: Technology and Applications. (Springer, 2008), pp. 6– 8
- S. Song, J. Xu, and R. K. Wang, Biomedical optics express 7, 4734 (2016).
- 11. M. C. Huang, Y. Zhou, and C. J. Chang-Hasnain, Nature photonics 1, 119 (2007).
- B. Potsaid, V. Jayaraman, J. G. Fujimoto, J. Jiang, P. J. Heim, and A. E. Cable, in (International Society for Optics and Photonics, 2012), 8213, p. 82130M.
- 13. S. Moon and E. S. Choi, Biomedical optics express 8, 1110 (2017).
- J. Xu, C. Zhang, J. Xu, K. Wong, and K. Tsia, Optics letters 39, 622 (2014).
- 15. M. Siddiqui, A. S. Nam, S. Tozburun, N. Lippok, C. Blatter, and B. J. Vakoc, Nature photonics 12, 111 (2018).
- R. Huber, M. Wojtkowski, and J. Fujimoto, Optics express 14, 3225 (2006).
- 17. T. DiLazaro and G. Nehmetallah, Optics Express 26, 2891 (2018).
- 18. O. M. Carrasco-Zevallos, C. Viehland, B. Keller, R. P. McNabb, A. N. Kuo, and J. A. Izatt, Biomedical optics express 9, 5052 (2018).
- J. Sun, E. Timurdogan, A. Yaacobi, E. S. Hosseini, and M. R. Watts, Nature 493, 195 (2013).
- 20. M. J. Heck, Nanophotonics 6, 93 (2017).
- 21. G. J. Tearney, R. Webb, and B. Bouma, Optics letters 23, 1152 (1998).
- 22. M. Okano and C. Chong, Optics Express 28, 23898 (2020).
- 23. International Electrotechnical Commission, IEC 60825-1 (2007).
- 24. S. Kakuma, Optical Review 24, 39 (2017).

#### References with titles

- J. Riemensberger, A. Lukashchuk, M. Karpov, W. Weng, E. Lucas, J. Liu, and T. J. Kippenberg, "Massively parallel coherent laser ranging using a soliton microcomb," Nature 581, 164–170 (2020).
- A. Dieckmann, "FMCW-LIDAR with tunable twin-guide laser diode," Electronics Letters 30, 308–309 (1994).
- M.-C. Amann, T. M. Bosch, M. Lescure, R. A. Myllylae, and M. Rioux, "Laser ranging: a critical review of unusual techniques for distance measurement," Optical engineering 40, 10–19 (2001).
- G. Berkovic and E. Shafir, "Optical methods for distance and displacement measurements," Advances in Optics and Photonics 4, 441–471 (2012).
- B. Behroozpour, P. A. Sandborn, M. C. Wu, and B. E. Boser, "Lidar system architectures and circuits," IEEE Communications Magazine 55, 135–142 (2017).
- X. Zhang, J. Pouls, and M. C. Wu, "Laser frequency sweep linearization by iterative learning pre-distortion for FMCW LiDAR," Optics express 27, 9965–9974 (2019).
- D. J. Lum, S. H. Knarr, and J. C. Howell, "Frequency-modulated continuous-wave LiDAR compressive depth-mapping," Optics express 26, 15420–15435 (2018).
- 8. R. Qian, K. C. Zhou, J. Zhang, C. Viehland, A.-H. Dhalla, and J. A. Izatt, "Video-rate high-precision time-frequency multiplexed 3D coherent ranging," Nature Communications **13**, 1476 (2022).
- 9. J. A. Izatt, M. A. Choma, and A.-H. Dhalla, "Theory of optical coherence tomography," in *Optical Coherence Tomography: Technology and Applications.* (Springer, 2008), pp. 6–8.
- S. Song, J. Xu, and R. K. Wang, "Long-range and wide field of view optical coherence tomography for in vivo 3D imaging of large volume object based on akinetic programmable swept source," Biomedical optics express 7, 4734–4748 (2016).
- M. C. Huang, Y. Zhou, and C. J. Chang-Hasnain, "A surfaceemitting laser incorporating a high-index-contrast subwavelength grating," Nature photonics 1, 119–122 (2007).
- B. Potsaid, V. Jayaraman, J. G. Fujimoto, J. Jiang, P. J. Heim, and A. E. Cable, "MEMS tunable VCSEL light source for ultrahigh speed 60kHz-1MHz axial scan rate and long range centimeter class OCT imaging," in (International Society for Optics and Photonics, 2012), Vol. 8213, p. 82130M.
- S. Moon and E. S. Choi, "VCSEL-based swept source for low-cost optical coherence tomography," Biomedical optics express 8, 1110–1121 (2017).
- J. Xu, C. Zhang, J. Xu, K. Wong, and K. Tsia, "Megahertz all-optical swept-source optical coherence tomography based on broadband amplified optical time-stretch," Optics letters 39, 622–625 (2014).
- M. Siddiqui, A. S. Nam, S. Tozburun, N. Lippok, C. Blatter, and B.
  J. Vakoc, "High-speed optical coherence tomography by circular interferometric ranging," Nature photonics 12, 111–116 (2018).
- R. Huber, M. Wojtkowski, and J. Fujimoto, "Fourier Domain Mode Locking (FDML): A new laser operating regime and applications for optical coherence tomography," Optics express 14, 3225–3237 (2006).
- T. DiLazaro and G. Nehmetallah, "Large-volume, low-cost, highprecision FMCW tomography using stitched DFBs," Optics Express 26, 2891–2904 (2018).
- O. M. Carrasco-Zevallos, C. Viehland, B. Keller, R. P. McNabb, A. N. Kuo, and J. A. Izatt, "Constant linear velocity spiral scanning for near video rate 4D OCT ophthalmic and surgical imaging with isotropic transverse sampling," Biomedical optics express 9, 5052–5070 (2018).

- J. Sun, E. Timurdogan, A. Yaacobi, E. S. Hosseini, and M. R. Watts, "Large-scale nanophotonic phased array," Nature 493, 195–199 (2013).
- M. J. Heck, "Highly integrated optical phased arrays: photonic integrated circuits for optical beam shaping and beam steering," Nanophotonics 6, 93–107 (2017).
- G. J. Tearney, R. Webb, and B. Bouma, "Spectrally encoded confocal microscopy," Optics letters 23, 1152–1154 (1998).
- M. Okano and C. Chong, "Swept Source Lidar: simultaneous FMCW ranging and nonmechanical beam steering with a wideband swept source," Optics Express 28, 23898–23915 (2020).
- International Electrotechnical Commission, "Safety of laser products-Part 1: Equipment classification and requirements," IEC 60825-1 (2007).
- S. Kakuma, "Frequency-modulated continuous-wave laser radar using dual vertical-cavity surface-emitting laser diodes for realtime measurements of distance and radial velocity," Optical Review 24, 39–46 (2017).

G GROUP